Available online at www.sciencedirect.com

ScienceDirect

Ceramics International 35 (2009) 747–753

CERAMICS INTERNATIONAL

www.elsevier.com/locate/ceramint

Pore geometry of 3D-C_f/SiC composites by mercury intrusion porosimetry

Wei Li *, Zhao Hui Chen

State Key Laboratory of Advanced Ceramic Fibers & Composites, College of Aerospace and Materials Engineering, National University of Defense Technology, Changsha 410073, PR China

Received 27 August 2007; received in revised form 15 November 2007; accepted 8 February 2008

Abstract

The 3D-C_f/SiC composites fabricated via precursor infiltration and pyrolysis (PIP) are porous inside due to their specific processing. To evaluate the porosity of 3D-C_f/SiC, a novel procedure of mercury intrusion porosimetry (MIP) was adopted to extract information from the hysteresis and entrapment. This method is able to eliminate the temporarily retained Hg at atmospheric pressure from the real entrapment due to topological reasons. From the interpretation of the MIP primary and secondary intrusion–extrusion data, accompanied by scanning electron microscopy (SEM) analysis and bubble point measurement, the pore geometry of 3D-C_f/SiC is supposed to be a 3D network originating from the architecture of braided carbon fabrics. This network is composed of hundreds of micron-sized large chambers between bundles, micro-cracks below 0.1 μm and medium-sized channels about 20–4 μm that bridge the former two and provide passages for fluids permeating the material.

Keywords: B. Porosity; CMCs; 3-Dimensional reinforcement; Analytical model; Mercury intrusion

1. Introduction

Precursor infiltration and pyrolysis (PIP) is one of the most important fabrication processes for 3-dimensional carbon fabric reinforced SiC (3D-C_f/SiC) composites. However, due to the pyrolysis gas escape and incomplete precursor infiltration, there are inevitably some voids and cracks in the 3D-C_f/SiC even after successive infiltration–pyrolysis cycles. Thus, the 3D-C_f/SiC composites are not totally dense but actually porous. This specific microstructure has critical influence on C_f/SiC mechanical and thermal properties [1,2], thus its evaluation is attractive and valuable undoubtedly. For fibers reinforced composites (FRC), scanning electron microscopy (SEM) is prevalently used to characterize the inner morphology [3,4], however, it is difficult to evaluate the porosities of the composites by SEM only, for its 2-dimensional, limited sight-fields.

For porous media, especially solids, mercury intrusion porosimetry (MIP) and isothermal N_2 sorption (INS) are the two classic methods to characterize the porosity, specific surface area, pore size distribution (PSD), and the surface roughness/surface fractal dimensions etc. [5,6]. Examples of the characterization of FRC by MIP are also reported [7,8]. The interpretation of MIP results is based on the Washburn equation [9], under the assumption that the pores are bundles of capillaries with various sizes which are equally accessible to the exterior mercury reservoir. The deviation of real cases from the above simplified model results in the intrusion–extrusion hysteresis and mercury entrapment. Several explanations have been offered to account for these phenomena, the most accepted one is the so-called ‘‘ink-bottle’’ effect [10] i.e., the pores' chambers are surrounded by smaller pore throats and access to the outside via them. Due to the shielding of throats on chambers, intrusion hysteresis occurs and the calculated PSD will be biased towards smaller than actual status, thus is also called the pore throat size distribution (PTSD). With the MIP becoming popular in many fields, this throat-chamber model faces increasing challenges and some new concepts have been raised to describe the complicated experimental results, e.g., the hysteresis of MIP is separated to ‘‘structural hysteresis'' and the ‘‘parametric hysteresis'' [11], according to their sources. The former is caused by the connectivity of pore network and

---

* Corresponding author. Tel.: +86 731 4576397; fax: +86 731 4573165.
E-mail address: superconductor1979@yahoo.com.cn (W. Li).

0272-8842/$34.00 © 2008 Elsevier Ltd and Techna Group S.r.l. All rights reserved.
doi:10.1016/j.ceramint.2008.02.011

the inter-shielding status of the large and small pores, reflecting the media's topological characters [12], while the latter is referred to the ones caused by the variation in contact angles, surface tensions during mercury advancing or retreating from the samples, and can be eliminated by adjusting the extrusion contact angles carefully [13]. The permanent mercury entrapment is believed to occur in the large pores shielded by the small ones, caused by the snap-off of mercury flow at the pore throats when retreating from the chambers [14], which is more likely to happen if the chamber/throat size ratio reaches 6 or higher [15].

MIP is an indirect characterization and the interpretation of the experimental data needs some theories and well-established models. Moreover, to extract more useful porosity information, specific operations are often applied during usual MIP procedure, among which applying secondary intrusion–extrusion after the primary cycle is the most familiar. This application can help to estimate the contribution of the shielded pores to mercury entrapment, evaluate the structures' damage of the samples induced by high pressures during intrusion, and distinguish the continuous, accessible parts of all the pore network that is crucial to permeability [16–18]. According to the previous literature, during MIP procedure, the re-intrusion started immediately as soon as the pressures reduced to a low level where the primary extrusion came to an end. However, to avoid dangers and damages upon apparatus, the primary/1st extrusion can only be carried out in the high-pressure ports, which determines the end pressure is higher than atmospheric pressure, e.g., 29 psia [18], or 250 psia [16]. Obviously, these pressures are not low enough to let the mercury retreat thoroughly, and mercury droplets will still retain in the large pores, which is immingled with the ''real'' entrapment.

Our preliminary work has shown that MIP is preferable to INS for characterization the porosity of 3D-C_f/SiC composites, because of the limited probing ranges and disability to macropores (>1 μm) of INS [19]. In this work, a novel secondary mercury intrusion–extrusion procedure was conducted to 3D-C_f/SiC besides the primary, to investigate the actual porosity of the composites. By interpreting the differences between these two MIP cycles, supported by SEM and bubble point method results, the pore geometry was analyzed and described.

2. Materials and methods

The 3D-C_f/SiC specimens were produced by subjecting the braided 3-dimensional carbon fiber fabrics (T300, Toray Inc., Japan) to some infiltration–pyrolysis cycles, using polycarbosilane (PCS) as the polymer precursor. To track the microstructural evolution of C_f/SiC, specimens underwent various fabricating cycles before finish were also chosen for characterization.

All MIP measurements were carried out with Micromeritics AutoporeIII 9420. Prior to characterization, the 3D-C_f/SiC specimens were sliced into segments about 4 cm × 4 cm to expose the inner pores. After repeated impregnation with ethanol, cleanout, and drying, some of these segments were loaded into the penetrometer, undergoing evacuation and pressurization at the low pressure port and the high one respectively, the pressures range from 1 to 55,000 psia ($6.9 \times 10^{-3} \sim 380$ MPa). Usually, the mercury extrusion begins as the pressure reaches the highest value and continues till the atmospheric pressure level (36 psia) reached. However, to make Hg withdraw from the samples as much as possible, a novel procedure was adopted. Firstly, the penetrometer was extracted from the high-pressure port when the 1st extrusion ended, then the sample segments were taken out carefully, loaded into another new penetrometer, evacuated to a very low pressure (5.3 Pa), and were subjected to the next intrusion–extrusion cycle. The raw data of 2nd MIP were adjusted by the original sample mass. The contact angle of Hg on the specimens during intrusion was assumed to be 130°, and its surface tension was 0.485 N/m. The equilibration time was 15 s both at intrusion and extrusion. The morphology of specimens cross-section was characterized by scanning electron microscope (JSM-5600LV, JEOL). The pore size and distribution was also characterized by the bubble point method according to the GB/T 5249-1985, GB/T 5250-1993 standards (PR China), applying ethanol as the saturation liquid.

3. Results and discussion

3.1. Capillary pressure curve

The primary and secondary MIP capillary pressure curves of 3D-C_f/SiC are plotted in Fig. 1. On the primary intrusion curve, there are several phases distinguished by different slopes. At the beginning of 1st extrusion, Hg does not retreat from the sample until the pressure reduces to the value of 0.2 μm-sized capillary, thus the extrusion branch lies above the intrusion one. With depressurization continuing, the extrusion's deviation from intrusion becomes wider and wider, till the pressure reaches the ambient level and retreating finishes. At the low capillary pressures below 20 μm, the 2nd intrusion curve is well consistent with the former one, but drops behind at higher

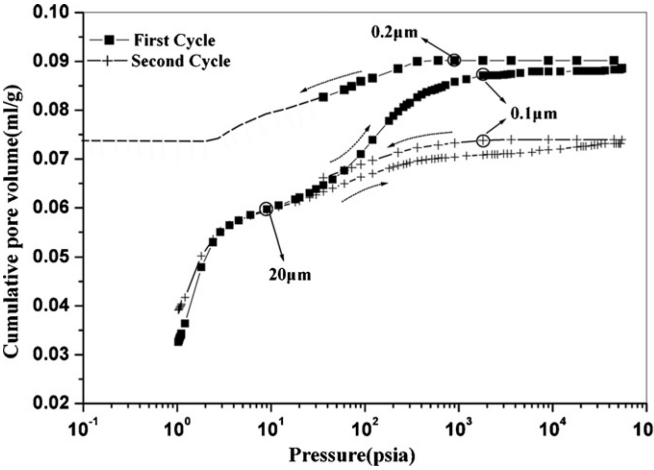

Fig. 1. Capillary pressure curves of 3D-C_f/SiC after primary and secondary MIP cycles, respectively. The dash line shows the possible trend of the 1st extrusion plot if the pressures keep reducing.

pressures and becomes horizontal gradually. The highest cumulative Hg volume intruded is only 80 vol.% of the former, i.e., 20% pores in the specimens are inaccessible for 2nd intrusion. As mentioned before, the evacuation before the 2nd intrusion starting can make the Hg withdraw from the pores free of shielding as much as possibly, hence the Hg only intrudes into the pores that are not occupied by the entrapped Hg after the last extrusion [16], and the disparity between the total Hg volumes of the 1st and 2nd intrusion reflects the amount of the entrapped Hg. Though not significant, the hysteresis still exists between the 2nd extrusion and intrusion, and the extrusion branch is similar and parallel to the former. These obvious hysteresis and Hg entrapment of 3D-C_f/SiC implies the heterogeneity of inside pores in a wide domain and the complicated connectivity of the system, according to the aforementioned theories about MIP mechanism.

3.2. Pore size distribution (PSD)

The pore size distribution of 3D-C_f/SiC is defined as the pore volume increments per unit logarithm of pore diameter vs corresponding pore diameters *D*, i.e., d*V*/d(log *D*) vs *D*, as plotted in Fig. 2. Obviously, there are several key diameters on the 1st intrusion PSD curve, i.e., 20 μm, 1.5 μm and 0.1 μm, dividing the curve into three parts. The first is above 20 μm, especially at 100 μm around, whose increasing rate is the highest, corresponding to the high slope of intrusion plot in Fig. 1, which implies the great volume contents of the large pores about hundreds of microns. After the first peak at 100 μm, the PSD curve declines drastically with the pressure increasing, till 20 μm, the d*V*/d(log *D*) reaches a relative low value. A convergent structure of pore is proposed to explain this trend, which restricts the Hg when its meniscus is advancing to the narrow throats, e.g., 20 μm-sized, and the increments reduce consequently. Another peak on PSD appears at 1.5 μm, with lower height but wider range (20–0.1 μm), than the first one at 100 μm. The last phase is below 0.1 μm, and the intrusion increments are quite small, indicating the stability of cumulative Hg volumes intruded and corresponding to the horizontal part of the capillary pressure curve in Fig. 1. According to traditional analysis, this kind of the PSD curve implies the pores in 3D-C_f/SiC possess two main components: one are hundreds of microns-sized large pores, and the other are the smaller ones about 20–0.1 μm. While the trend of extrusion will be interpreted as the shielding effects of 0.2 μm pores leading to the surface on the smaller ones, from the "structural hysteresis" points of view.

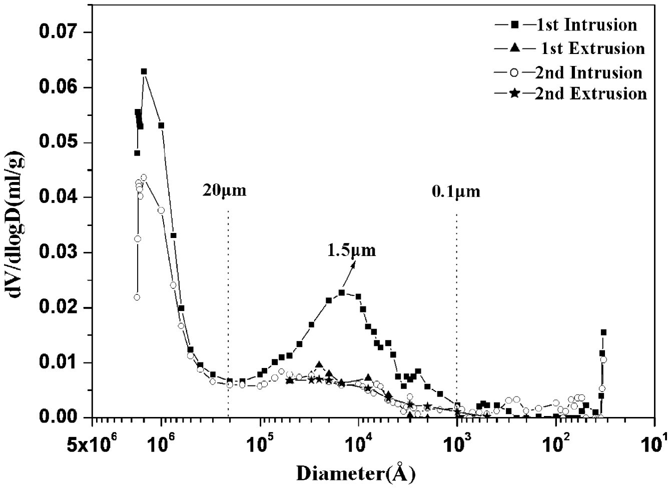

Fig. 2. Pore size distribution (PSD) curves of 3D-C_f/SiC from the two MIP cycles. The extrusion data are plotted negatively for convenience of comparison.

As for the 2nd cycle, the intrusion PSD shows a similar peak style above 20 μm with the first. Hence, it is reasonable to believe that the intrusion in the pores of these sizes is reversible, the Hg can retreat from these large pores thoroughly, and they are free from shielding but leading to the surface directly. By comparison with SEM image of morphology of 3D-C_f/SiC in Fig. 3, these large pores are quite matching with A-type pores that are chambers between the twisting bundles, both at sizes and locations.

While in the range of 20–0.1 μm, the Hg increments of 2nd intrusion are much lower than the 1st ones, and the second peak has almost disappeared at 1.5 μm on the curve. From the analysis of the capillary pressure curves above, it has been known that the content of the entrapped Hg adds up to 20 vol. % of the total intruded at 1st intrusion. Now, it is clear that the entrapment occurs in the pores whose nominal sizes dwell in 20–0.1 μm during the 1st extrusion. The exact porous structure where the Hg remains can be spotted by focusing on the carbon fabrics, for their architecture is one of the main determinants of as-produced 3D-C_f/SiC's porosity. The longitudinal size of the stitch of 3D-braided fabric adopted in this paper is about 5.5 cm, to which the length of the specimens sliced is comparable (4–5 cm), thus the A-type large pores on the surfaces of specimens are not individual but repeated inside. One can imagine, if the applied pressure breaks through the threshold of throat, e.g., 20 μm-sized, the mercury will rush into the large chambers inside massively, but this volume will only be attributed to the 20 μm or smaller pores automatically, that is what has happened on the PSD of 1st intrusion. While

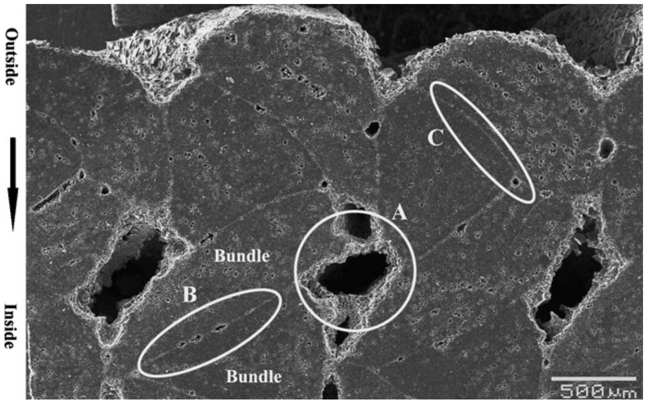

Fig. 3. Morphology of the cross-section of 3D-C_f/SiC by SEM. Type A represents the inter-bundle large chambers exposed by slicing. Types B and C are both paths between the bundles, and C leads to the sample's surface, connecting the inside and the outside of the sample.

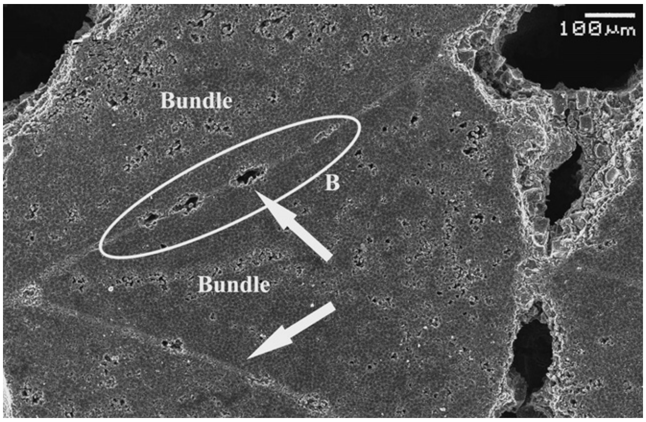

Fig. 4. The paths between the carbon bundles. The arrows indicate the paths that are not fully blocked by matrix. Area B refers to the same location in Fig. 3.

extrusion starts, the Hg flow retreats from the chambers via the throats, and tends to snap-off for the great disparity of their sizes from hundreds of microns to 20 µm or less, thus some Hg retained and entrapment occurs, according to the relevant theories [14]. Therefore, the real sites of entrapment among 20–0.1 µm is the inside large chambers between bundles, while they are shielded by narrower throats, which is different from the exposed ones. Hence, the left of the 1st extrusion curve can be deduced as the dash line in Fig. 1, providing the pressures are reduced continuously from the atmospheric value.

Also in 20–0.1 µm range, the 1st extrusion, 2nd intrusion and 2nd extrusion overlap each other on the whole, without any hysteresis or entrapment. This phenomenon implies that the Hg flow can move reversibly in these pores of 20–0.1 µm, which are free from the effects of shielding or heterogeneity of sizes.

Below 0.1 µm in Fig. 2, though very small, the hysteresis does exist between the intrusion and extrusion both in 1st and 2nd cycle, while the entrapment is not observed. The starting point of 2nd extrusion is 0.1 µm, which is similar to the 1st one's.

According to all the analysis above, it is clear that there are some special pores with multiple functions in 3D-C_f/SiC, whose sizes are in the range of 20–0.1 µm. On one hand, these pores act as the throats at the ends of the convergent large chambers of hundreds of microns, limiting and joining them, on the other hand, they connect and shield the small pores under 0.1 µm. Meanwhile, these pores lead to the sample surface, allowing the Hg flowing unrestrictedly and reversely. Thus, these pores integrate the others, and a 3D porous network comes into being inside the 3D-C_f/SiC. From the micrograph of the morphology (Fig. 3), there are apparent paths at the borders of adjacent bundles, some connect the inter-bundle chambers, e.g., type B, and others join the chambers indirectly via else paths, e.g., type C. Especially, type C paths reside near the surface and lead to the outside. These paths connect each other, spread inside and make a path tree. As the SEM images shown in Fig. 4, these paths are not fully blocked by the filled matrix like the area B, but include mass openings and micro-channels, owing to the incomplete infiltration or micro-cracks derived from the pyrolysis of precursor. Hence, they are called channels inside, whose maximum sizes are about 10–20 µm. From the point of configuration and sizes, these channels both resemble the special pores in 20–0.1 µm range that are deduced from the MIP results. Therefore, it is reasonable to suppose that the channel network plays an important role in 3D-C_f/SiC.

Like MIP, bubble point method is also an intrusion method, while it can only characterize those pores which are always open throughout the samples, and its data reflect the narrowest parts' sizes of the pores. Fig. 5 shows the cumulative volume curve and PSD of 3D-C_f/SiC obtained via this method. It can be seen that the pores' sizes distribute concentratively. Most of the open pores (>95 vol.%) are 0.3–0.4 µm-sized, and the single peak on PSD curve appears at 0.35 µm, while the first bubble emerged at 2.7 µm, the maximum throat's size. By comparison, the range of PSD by bubble point method is only a small part of the one by MIP, which implies that minority pores of total are full-open actually. Obviously, the full-open pores' size is in the range of the inter-bundle channels (20–0.1 µm), and is especially close to the critical pore sizes of the mercury extrusion (0.1–0.2 µm). This result proves that the channels can provide the passage through which the fluids flow across the sample on percolation mechanism, and their throat size determines the difficulty of flowing, e.g., the type C channel in Fig. 3 controls the threshold pressure at which the fluids can penetrate into the samples.

3.3. *Evolution of porosity*

To investigate the formation and evolution of the complicated porosity of 3D-C_f/SiC, the partially densified specimens at intermediate stages, i.e., enduring various PIP recycles, were also characterized by MIP, the results are plotted in Figs. 6 and 7.

In Fig. 6, the total intrusion volume of 3PIP 3D-C_f/SiC is much higher than the finished, and the profile of the former's PSD curve is also different from the latter. The first peak lies from above 100–40 µm, which is caused by the exposed inter-bundle chambers, the second peak reflects the summation of the volumes of the inter-bundle channels and the chambers shielded by them, while it has much higher increments than

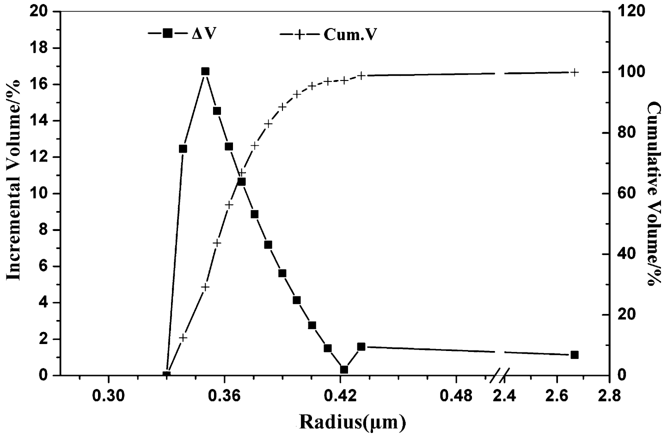

Fig. 5. Cumulative volume curve and PSD of 3D-C_f/SiC by bubble point method.

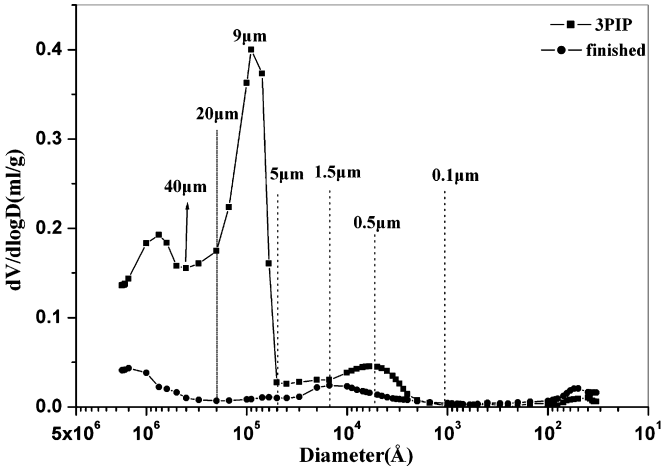

Fig. 6. PSD curves of the partially densified (after only 3 PIP recycles, 3 PIP) and finished 3D-C_f/SiC by MIP.

the first, which is opposite to the finished one. The critical sizes of the second peak are 40 μm and 5 μm, and the top point locates at 9 μm, which are all higher than those of the finished (20 μm, 0.1 μm and 1.5 μm). Apparently, at the beginning of fabrication, the densification of 3D-C_f/SiC has not been very high yet, and the inside pores (chambers, channels) are still large, due to the low percentage of the matrix filling. For instance, in Fig. 8, channel C links the exposed and inside chambers, whose smallest size reaches as high as 50 μm. Reasonably, the predominant content of 2nd peak can be attributed to the summed volumes of the channels and they shielded chambers, which even exceeds the volumes of the exposed chambers. With the fabrication continues, each kind of pores reduces in both sizes and contents (Fig. 7), and the aforementioned two peaks' heights and areas decrease simultaneously, the critical peaks' sizes move towards the low level and have become stable since now. Moreover, at about 4–5 μm, the PSD curves of specimens after 7–10 PIP cycles (7–10 PIP specimens) all present a weak fluctuation, splitting the peak among 20–0.1 μm into two. And the denser the specimens are, the weaker this form becomes. At 14th PIP, it has become too faint to distinguish. One speculation about this splitting is that 4–5 μm is the dividing line of the channel's size and the chamber's, i.e., the intrusion volume among 20–4 μm belongs to channels, while the one among 4–0.1 μm belongs to the chambers being shielded, actually. According to this assumption, in Table 1, the pores above 0.1 μm are separated into three categories, and their contents' evolution is presented also. It is clear that the channels' volumes are lower than those of the shielded chambers and only amount to approximately one third of the latter's. Both volumes of the channels (20–4 μm) and the shielded chambers (4–0.1 μm) decrease with fabrication proceeding, but their volume ratio is maintained. However, the volume variations of the uncovered large chambers (>20 μm) are not so regular, which is attributed to the heterogeneity of the specimens' surfaces derived from the random slicing of the samples. The 3D-C_f/SiC after 14 PIP cycles were characterized twice, the second measurement includes the additional re-injection and re-extrusion of Hg. These characterizations have good reproducibility among 20–0.1 μm, which indicates the reliability and precision of MIP results.

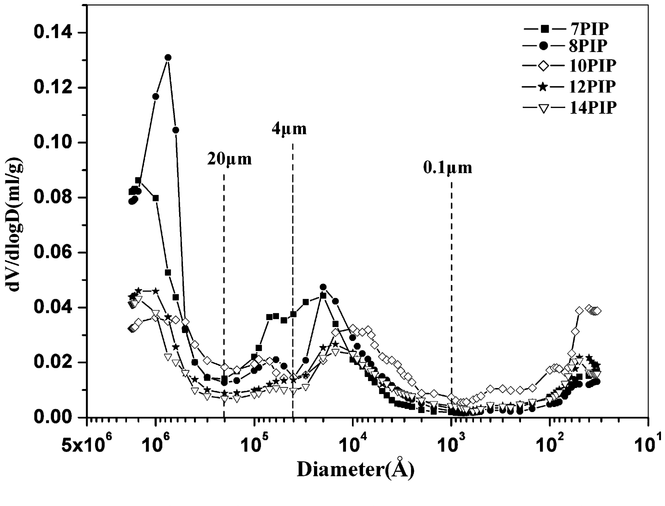

Fig. 7. Evolution of PSD of partially densified 3D-C_f/SiC with the fabrication continuing (from 7 to 14 PIP cycles).

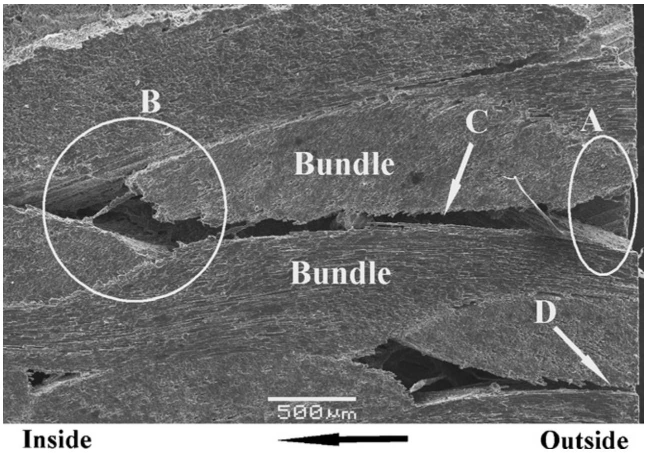

Fig. 8. Longitudinal cross-section of 3D-C_f/SiC at the initial fabrication by SEM. Symbol A represents the pore chamber at the surface, B is the inside one, C and D are both channels between bundles, and D leads to the outside of sample directly.

Table 1

Contents of pores with different sizes from mercury intrusion data of 3D-C_f/SiC at different fabrication stages

Stage	Pore volumes (ml/g)		
	>20 μm	20–4 μm	4–0.1 μm
7 PIP	0.0445	0.0186	0.0299
8 PIP	0.0613	0.0118	0.0314
10 PIP	0.0293	0.0124	0.0318
12 PIP	0.0261	0.00760	0.0234
14 PIP-1[a]	0.0217	0.00610	0.0220
14 PIP-2-1st[b]	0.0597	0.00610	0.0213
14 PIP-2-2nd[c]	0.0594	0.00464	0.00683

[a] the no. 1 MIP measurement.

[b] primary intrusion of the no. 2 measurement.

[c] re-injection of the no. 2 measurement.

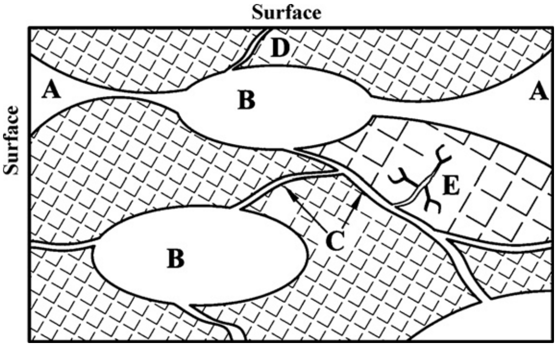

Fig. 9. Physical model 3D-C_f/SiC for fluids invasion. Symbol A represents the inter-bundle chamber exposed by slicing, Symbol B refers to that shielded by channel, as C pointed out. D is the channel that leads to the surface directly. E represents a group of micro-cracks which connects with channels and will be shielded by them during extrusion of MIP.

Back to the PSD curve of 3D-C_f/SiC after 3 PIP cycles in Fig. 6, the 3rd peak locating at 1.5–0.1 μm, which is not observed since the 7th PIP cycle, is supposed to be covered into the plot among 4–0.1 μm, due to the pores becoming smaller.

3.4. Pore geometry of 3D-C_f/SiC

Based on the interpretation of MIP data and analysis of SEM images above, a rough depiction about the pore geometry of 3D-C_f/SiC is deduced, as the Fig. 9 shown. In 3D-C_f/SiC, there is a complicated 3-dimensional pore network, which originates mainly from the architectures of the braided carbon fabrics. This network includes several main components. The most important are the channels at the bundles' borders with sizes about 4–20 μm (symbols C and D), making up the skeleton of porosity, connecting the bigger and smaller pores, and offer passages for fluids' flowing directly or via percolation mechanism. Another are the inter-bundle chambers (symbols A and B), with size of hundreds of microns, and they are the reservoirs of fluids. The last one, from the MIP results, are pores below 0.1 μm, which are attributed to micro-cracks, e.g., inside the bulk matrix or near the fiber–matrix interface based on our preliminary results, and they also connect with the channels. Certainly, this model is only a simulation of the real status, and need further improvement and correction, for it neglects the regularity of pores' arrangement in the fabrics, and also omits the intra-bundle pores which are not distinguishable by MIP, and so on. However, our research provides some hints on the insights into the microstructure of 3D-C_f/SiC composites.

4. Summary

3D-C_f/SiC fabricated by PIP is a kind of porous material, because of its specific processing. MIP is an effective characterization method for porous media, nevertheless the porosity information from the raw data of MIP deviates from the actual cases, for the over-simplified model applied. To interpret MIP data accurately and gain more reliable description, additional theories and operations are needed. In this work, a novel secondary intrusion–extrusion cycle was adopted. Firstly, the penetrometer was extracted from the high-pressure port when the 1st extrusion ended, then the sample segments were taken out carefully, loaded into another new penetrometer, evacuated the penetrometer to a very low pressure (40 μm Hg, 5.3 Pa) and were subjected to the next intrusion–extrusion cycle. Through this operation, Hg is able to withdraw from the samples as much as possible, eliminating the temporarily retained Hg at atmospheric pressure from the real entrapment due to topological reasons. From the interpretation of the MIP results according to the models of hysteresis and Hg entrapment, accompanied by SEM analysis and bubble point measurement, a model to describe the porosity of 3D-C_f/SiC is proposed. In 3D-C_f/SiC, a 3-dimensional network of pores exists, which originates mainly from the architectures of the braided carbon fabrics. This network includes several main components. The most important are the channels at the bundles' borders with sizes about 4–20 μm, making up the skeleton of porosity, communicating with the bigger or smaller pores, and offering passages for fluids' flowing. Another are the inter-bundle chambers, with size of hundreds of microns, which are the reservoirs of fluids. The last ones are the pores below 0.1 μm, which are attributed to micro-cracks, e.g., inside the bulk matrix or near the fiber–matrix interface. This model provides preliminary understanding of the 3D-C_f/SiC's porosity. A more accurate model by means of network modeling or fractal geometry theory is under research at present for simulating the fluids flow in the 3D-C_f/SiC.

Acknowledgements

We would like to thank Mr. H. T. Zhang (China Building Materials Academy, CBMA) and Mr. D. W. Chang (Tsinghua University) for their great help on MIP measurements and also valuable advices.

References

[1] S.R. Qiao, S.M. Du, G.C. Ji, et al., Damage mechanism of 3D-C/SiC composite, J. Mechan. Strength 6 (2004) 307–312.
[2] D.P.H. Hasselman, Effect of cracks on thermal conductivity, J. Compos. Mater. 12 (1978) 403–407.
[3] S.M. Dong, Y. Katoh, A. Kohyama, et al., Microstructural evolution and mechanical performances of SiC/SiC composites by polymer impregnation/microwave pyrolysis (PIMP) process, Ceram. Int. 28 (2002) 899–905.
[4] W. Krenkel, Microstructure tailoring of C/C-SiC composite, Ceram. Eng. Sci. Proc. 24 (2003) 471–476.
[5] C.A.L. León, New perspectives in mercury porosimetry, Adv. Colloid Interf. Sci. 76–77 (1998) 341–372.
[6] L.B. Liu, X.H. Wang, Fractal analysis of bentonite porosity using nitrogen adsorption isotherms, J. Chem. Eng. Chin. Univ. 17 (2003) 591–595.
[7] S. Suyama, T. Kameda, Y. Itoh, Evaluation of microstructure for SiC/SiC composites, Int. J. Mater. Prod. Tech. 16 (2001) 232–238.
[8] S. Suyama, Y. Itoh, Evaluation of microstructure for SiC/SiC composites using mercury intrusion method, Ceram. Eng. Sci. Proc. 20 (1999) 181–189.
[9] E.W. Washburn, The dynamics of capillary flow, Phys. Rev. 17 (1921) 273–283.
[10] F. Moro, H. Böhni, Ink-bottle effect in mercury intrusion porosimetry of cement-based materials, J. Colloid Interf. Sci 246 (2002) 135–149.

[11] S.P. Rigby, R.S. Fletcher, S.N. Riley, Characterisation of porous solids using integrated nitrogen sorption and mercury porosimetry, Chem. Eng. Sci. 59 (2004) 41–51.

[12] G.R. Wang, Study on Pore Structure of Porous Materials under Diffusion/Reaction Conditions, Tianjing University, Tianjing, 2000.

[13] C. Salmas, G. Androutsopoulos, Mercury porosimetry: contact angle hysteresis of materials with controlled pore structure, J. Colloid Interf. Sci. 239 (2001) 178–189.

[14] F. Porcheron, P.A. Monson, Molecular modeling of mercury porosimetry, Adsorption 11 (2005) 325–329.

[15] G.P. Matthews, C.J. Ridgway, M.C. Spearing, Void space modeling of mercury intrusion hysteresis in sandstone, paper coating and other porous media, J. Colloid Interf. Sci. 171 (1995) 8–27.

[16] S.P. Rigby, D. Barwick, R.S. Fletcher, et al., Interpreting mercury porosimetry data for catalyst supports using semi-empirical alternatives to the Washburn equation, Appl. Catal. A 238 (2003) 303–318.

[17] S.P. Rigby, R.S. Fletcher, S.N. Riley, Determination of the cause of mercury entrapment during porosimetry experiments on sol–gel silica catalyst supports, Appl. Catal. A 247 (2003) 27–39.

[18] Z. Liu, D. Winslow, Sub-distribution of pore size: a new approach to correlate pore structure with permeability, Cem. Concr. Res. 25 (1995) 769–778.

[19] W. Li, Z.H. Chen, Characterization of partially densified 3D C_f/SiC composites by using mercury intrusion porosimetry and nitrogen sorption, Ceram. Int. 34 (2008) 531–535.